Electrical transport properties of micrometer-sized samples of the rare-earth chiral magnet $YbNi_3Al_9$

Ryuya Aoki,[1] Yoshihiko Togawa,[1,2] and Shigeo Ohara[3]

[1]*Department of Physics and Electronics, Osaka Prefecture University, Sakai, Osaka 599-8531, Japan*

[2]*Chirality Research Center (CResCent), Hiroshima University, Higashi-Hiroshima, Hiroshima 739-8526, Japan*

[3]*Department of Physical Science and Engineering, Graduate School of Engineering, Nagoya Institute of Technology, Nagoya 466-8555, Japan*

(Received 6 March 2018; revised manuscript received 17 May 2018; published 13 June 2018)

We investigate electrical transport properties of micrometer-sized samples of the rare-earth-based monoaxial chiral magnetic crystal $YbNi_3Al_9$ in order to characterize chiral magnetic structures. The magnetoresistance (MR) data exhibit discrete changes, supporting the formation of the chiral spin soliton lattice (CSL) in $YbNi_3Al_9$. Reversal and lock-in behavior of the MR signal are significant features during the CSL formation, which contrast with hysteresis behavior reported in a prototype monoaxial chiral magnetic crystal of $CrNb_3S_6$. The magnetic phase diagrams are provided based on the electrical transport properties in micrometer-sized $YbNi_3Al_9$ crystals.

DOI: 10.1103/PhysRevB.97.214414

I. INTRODUCTION

Chirality, derived from the Greek word "$\chi\varepsilon\iota\rho$" meaning the palm by Lord Kelvin, is one of the essential concepts of symmetry. It describes a geometrical relationship of materials in which the original object does not overlap its mirrored structure, as seen in paired structures such as left and right hands. Chirality plays an important role in determining physical properties of materials with chiral structures. In a field of magnetism, magnetic materials with chiral crystalline structures exhibit the Dzyaloshinskii-Moriya (DM) antisymmetric exchange interaction [1,2]. The DM exchange interaction competes with the Heisenberg symmetric exchange interaction and the Zeeman energy induced by magnetic fields in chiral magnetic materials, which results in the formation of nontrivial spin ordered structures, such as a chiral spin soliton lattice (CSL) [3–5] or a chiral magnetic skyrmion [6]. Indeed, these chiral spin ordered structures were observed in noncentrosymmetric magnetic crystals, as exemplified by $CrNb_3S_6$ [7], MnSi [8], and FeGe [9,10]. One of the most striking physical responses expected in chiral magnetic materials is the coupling of conduction itinerant spins with the chiral spin order of localized spins, causing unconventional magnetotransport properties such as discrete magnetoresistance (MR) [11] or the topological Hall effect [12]. Therefore, chiral magnetism has attracted a strong interest among the community of condensed matter physics and has been actively studied for exploring novel aspects of spin electronics utilizing advantageous properties of the chiral spin order.

Discretized physical responses are widely found in monoaxial magnetic crystals of $CrNb_3S_6$ [11,13–15] as well as in thin films of cubic B20 compounds such as MnSi [16] and FeGe [17]. This is due to the CSL formation in a finite-size system. Namely, the topological nature of the chiral solitons becomes prominent in a confinement geometry and induces the discretization effect of physical properties during the CSL formation. One of the effective methods of detecting the CSL formation is MR measurements. In a prototype monoaxial chiral magnetic crystal of metallic $CrNb_3S_6$, negative MR signals are observed with increasing magnetic field strength since each chiral soliton works as a magnetic potential for itinerant conduction spins and the scattering probability is well correlated with the soliton population. As a consequence, the behavior of MR is well fitted by the soliton density, which corresponds to the order parameter of the CSL formation. Moreover, when reducing the sample size along the helical c axis, discretized changes of the MR signals are noticeable with accompanying hysteresis. These features evidence the existence of CSLs in micrometer-sized $CrNb_3S_6$ crystals.

In the case of rare-earth intermetallic $Yb(Ni_{1-x}Cu_x)_3Al_9$, where Ni atoms are substituted with Cu atoms in the parent material $YbNi_3Al_9$, the CSL formation has been demonstrated recently by resonant x-ray scattering experiments [18] and specific heat measurements [19]. In resonant x-ray scattering experiments, it was observed that the magnitude of the propagation vector of the helicoidal order decreases with an increasing magnetic field applied perpendicularly to the helical c axis. This result provides a physical picture that the helicoidal order has a longer period at larger magnetic fields and is consistent with the behavior expected for the CSL formation. In addition, the plateau of the CSL period was observed in a particular range of magnetic fields while the magnetic field was swept and the CSL transformed its structure in $Yb(Ni_{1-x}Cu_x)_3Al_9$ crystals. This behavior was interpreted as a lock-in behavior of the CSL phase, as the CSL period matched the characteristic length of the crystal, which was consistent with a scenario recently proposed by variational calculations [20]. Specific heat measurements [19] also presented sharp peaks associated with the CSL formation in $Yb(Ni_{1-x}Cu_x)_3Al_9$. On the other hand, in the parent material $YbNi_3Al_9$, neutron [21] and resonant x-ray [18] scattering experiments clarified that the helical pitch L_0 is 3.4 nm at zero magnetic field with the propagation vector $\mathbf{q}_0 = (0,0,0.8)$ along the c^* direction. However, the CSL formation has not been observed in experiments described above [18,19]. The existence of chiral solitons and the CSL is still under investigation in $YbNi_3Al_9$.

TABLE I. Comparison between $YbNi_3Al_9$ and $CrNb_3S_6$.

	$YbNi_3Al_9$	$CrNb_3S_6$
Space group	$R32$	$P6_322$
Crystal class	Trigonal	Hexagonal
Magnetic atom	Yb	Cr
T_c (K)	3.4	127
c (Å)	27.3	12.1
L_0 (nm)	3.4	48
c/L_0	0.80	0.025

Interestingly, there are many differences in physical properties between $YbNi_3Al_9$ and $CrNb_3S_6$ crystals, as described in Table I. The former is a $4f$ electron system, while the latter is a $3d$ electron system. Thus, the microscopic origin of symmetric Heisenberg and antisymmetric DM exchange interactions should differ in each system. The helical pitch L_0 for $YbNi_3Al_9$ is much shorter than that for $CrNb_3S_6$. These features may influence significantly the scattering process of conduction electrons on chiral magnetic phases, which should be clarified for further understanding of chiral magnetism in the $4f$ electron system.

In this paper, we investigated the electrical resistance of micrometer-sized $YbNi_3Al_9$ samples at various temperatures and magnetic fields and clarified that the CSL formation occurs in $YbNi_3Al_9$ crystals. Section II describes details of fabricating specimens and experimental methods. Section III shows characteristics of the electrical resistance for $YbNi_3Al_9$ crystals. The MR data taken with a fine field interval present stepwise changes and lock-in behavior, suggesting the existence of the CSL. The magnetic phase diagram is derived from these data. Similarities and differences between the CSL formation in $YbNi_3Al_9$ and $CrNb_3S_6$ crystals are discussed. A summary is given in Sec. IV.

II. EXPERIMENTAL

$YbNi_3Al_9$ belongs to a family of rare-earth intermetallic compounds RNi_3Al_9 (R = Y, Gd, Dy, Er, and Yb). It takes an $ErNi_3Al_9$-type layer structure, namely a trigonal structure of the space group $R32$ [22]. Magnetic ions of Yb form a honeycomb array within the ab plane containing a triangular array of Al ions as shown in Figs. 1(a) and 1(b). This Yb_2Al_3 layer is followed by three stacking layers of a triangular lattice composed of Al and Ni ions. The size of the unit cell is 7.3 and 27.3 Å along the a and c axes, respectively. The distance between the nearest Yb atoms is 4.2 Å in the plane and 9.1 Å between the planes [23]. The helical magnetic order with a fixed direction of the spin rotation (chiral helimagnetic order) appears with $L_0 = 3.4$ nm below the transition temperature $T_c = 3.4$ K. The magnetic moments localized on Yb ions are aligned ferromagnetically within the ab plane and rotate along the helical c axis.

$YbNi_3Al_9$ bulk single crystals were grown by using an Al self-flux method [24]. Micrometer-sized platelet samples with a typical size of 10 μm × 10 μm × 0.5 μm were cut from the bulk single crystal and attached to Si substrates by Pt deposition using a focused ion beam (FIB) system. The electrodes (Ti/Au)

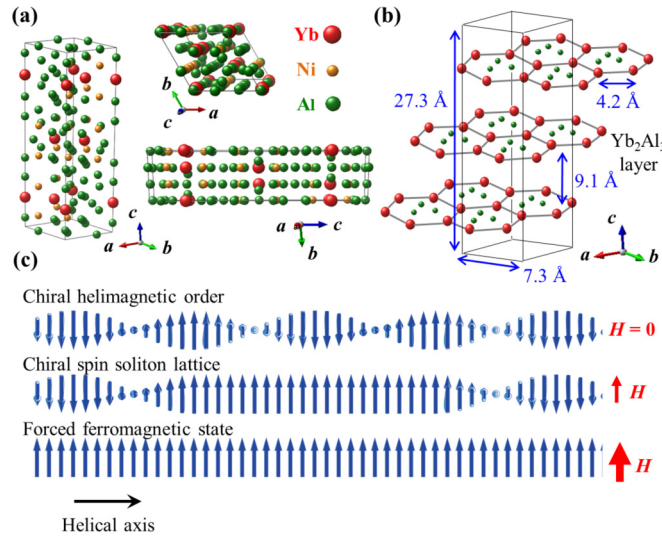

FIG. 1. (a) Overall, top, and side views of the crystal structure of $YbNi_3Al_9$. (b) Schematic of the Yb_2Al_3 layers structure. (c) Schematic of the chiral helimagnetic order, the chiral spin soliton lattice, and forced ferromagnetic phases.

were prepared on the edges of the platelet samples by using electron beam lithography and lift-off techniques.

Figures 2(a)–2(c) show the configurations of three samples examined in this study. The main difference is a geometrical relationship of the magnetic field, the current flow, and crystalline orientations. The numbers of helices at zero magnetic field are 150, 3000, and 3000 for samples 1, 2, and 3, respectively. The current flows in the direction parallel to the in-plane, namely CIP configuration in samples 1 and 2 as shown in Figs. 2(a) and 2(b), while sample 3 has the configuration with the current flowing perpendicular to the plane (CPP configuration) shown in Fig. 2(c). In addition, sample 1 has the smallest area of the sample plane perpendicular to the magnetic field, inducing a small demagnetization effect as seen below.

The electrical resistance was measured by a two-terminal method with an ac current (137 Hz) whose amplitude value was either 0.1 or 1 mA. No significant difference was found in the resistance taken at different values of the current, suggesting that no Joule heating occurred in this current regime. The temperature was varied from 1.9 to 298 K. In MR measurements, a magnetic field was applied perpendicularly to

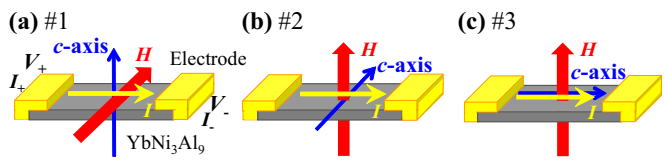

FIG. 2. Schematics of the sample configurations. Based on the sample dimensions and crystal orientation, the numbers of helices at zero magnetic field are 150, 3000, and 3000 for the samples 1, 2, and 3, respectively. The current mainly flows within the ab plane in samples 1 and 2 [current in-plane (CIP) configuration], and along the c axis in sample 3 [current perpendicular plane (CPP) configuration]. The demagnetization effect in sample 1 is smaller than that in samples 2 and 3.

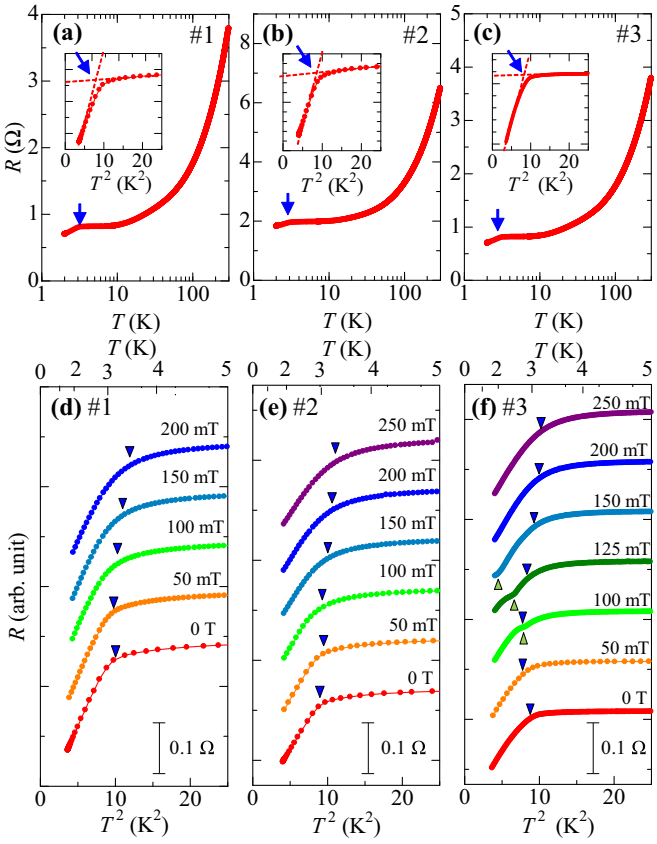

FIG. 3. (a)–(c) Temperature dependence of the electrical resistance of samples 1 to 3, respectively, at zero magnetic field plotted on a logarithmic scale. The insets show the electrical resistance against T^2 at low temperature. Blue arrows indicate the location of T_c. (d)–(f) The electrical resistance of samples 1 to 3 at various magnetic fields. The curves are vertically shifted by 0.1 Ω. The blue arrow-down heads indicate T_c and the green arrow-up heads indicate the onset of the kink structure observed in the presence of the magnetic field.

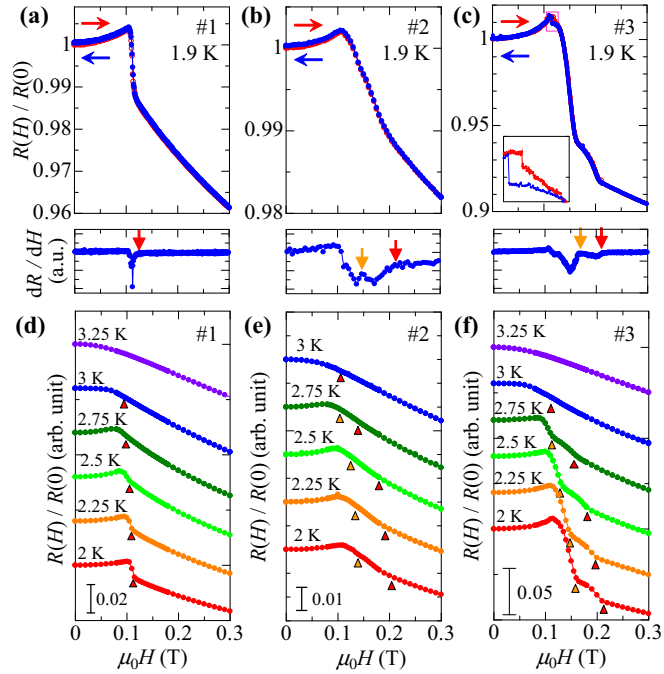

FIG. 4. (a)–(c) Normalized MR data and their derivative with respect to the magnetic field for the micrometer-sized $YbNi_3Al_9$ samples 1–3, respectively. The MR data given in red dots were taken at 1.9 K in the process of increasing the magnetic field, while those in blue solid dots were taken in the process of decreasing the magnetic field. The field increments of panels (a) and (c) are 1 mT, while that of panel (b) is 5 mT. The inset in panel (c) corresponds to an enlarged view of the MR data between 0.11 and 0.13 T, indicated by a magenta frame. The critical field H_c is determined by the starting point of monotonous negative MR at large field, as indicated by the red arrows. The onsets of a hump structure are indicated by orange arrow heads. (d)–(f) The dependence of MR data on temperatures between 2 and 3.25 K. The curves in panels (d) and (e) are vertically shifted by 4%, while those in panel (f) are vertically shifted by 2%.

the c axis of the samples and changed between zero and 0.3 T. In the configuration of sample 1, the demagnetization effect due to shape anisotropy is smaller than those found in other configurations. Thus, the value of the critical magnetic field for sample 1 is smaller than those for samples 2 and 3, as shown below.

III. RESULTS AND DISCUSSION

A. Temperature dependence of electrical resistance

Figures 3(a)–3(c) show the temperature dependence of the electrical resistance given in a logarithmic scale for samples 1 to 3, respectively. In samples 1 and 2, the current flows along the ab plane, while it flows along the c axis in sample 3. Since $YbNi_3Al_9$ forms a Fermi liquid, the electrical resistance is dominantly caused by electron-electron scattering and shows the T^2 dependence, as expressed by $\rho = \rho_0 + AT^2$. This behavior is indeed seen in the insets of Figs. 3(a)–3(c). A magnetic transition temperature of 3.05 K was obtained by extrapolating the low- and high-temperature regimes, as indicated in the insets of Figs. 3(a)–3(c). The obtained values are slightly smaller than T_c of the bulk crystal (3.4 K), possibly due to small contamination at the surface while preparing the specimen using FIB. Moreover, the reduction of the resistance with increasing temperature due to the Kondo effect, which was observed at temperatures between 30 and 100 K in bulk crystals with the current being perpendicular to the c axis [23,25], was largely suppressed in samples 1 and 2 with the corresponding configuration of the current and the c axis. However, to see the Kondo effect, the subtraction of the reference resistance data of a nonmagnetic material such as $LuNi_3Al_9$ is required as performed in the analysis of the bulk crystal.

The electrical resistance data as a function of temperature taken at various magnetic fields are shown in Figs. 3(d) to 3(f). The magnetic phase transition was observed in all samples as seen at zero magnetic field. The value of T_c moves toward higher temperature with an increasing magnetic field, as indicated by blue arrow-down heads. In sample 3, an additional feature of a kink structure appears below T_c in the presence of the magnetic field, the origin of which is discussed in the following paragraphs.

B. Magnetoresistance

Figure 4 shows the MR data at 1.9 K of the micrometer-sized $YbNi_3Al_9$ samples 1 to 3. At large fields, the MR signals vary monotonically with an almost fixed slope in all samples.

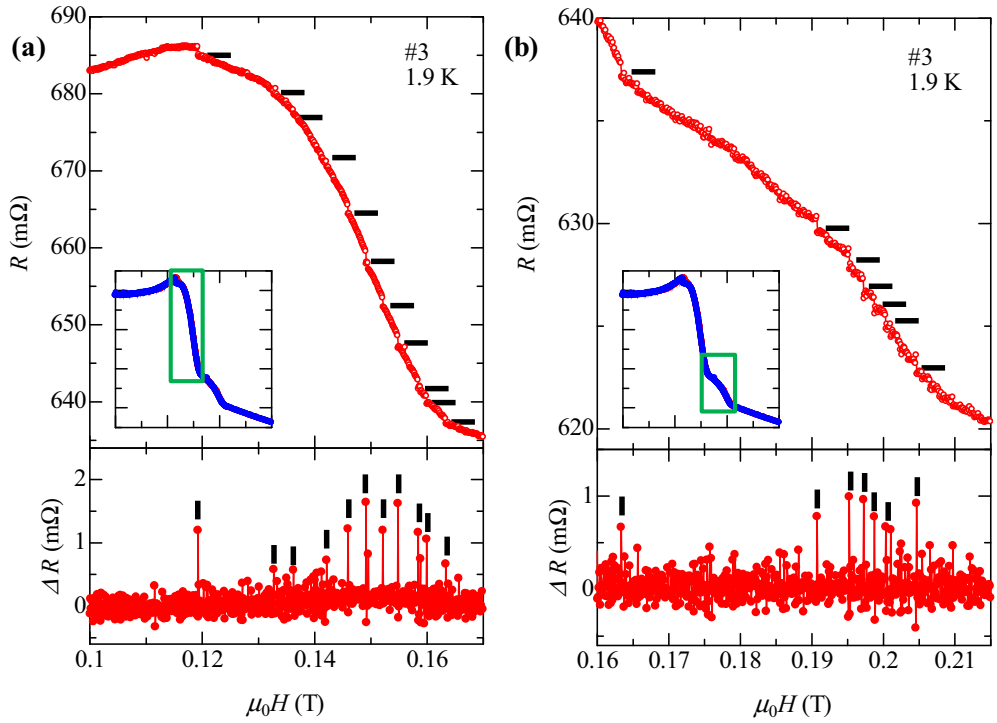

FIG. 5. MR data and their differential ΔR between neighboring data points in the process of increasing the magnetic field taken with a fine field increment of 0.1 mT for sample 3. Many stepwise changes of the MR signal are clearly found as indicated by black horizontal and vertical bars. (a) MR data in the field region before the hump structure appears. (b) MR data in the hump structure.

The critical field H_c was determined as the point where such a monotonic negative MR starts, as indicated by red arrows in the derivatives shown in Figs. 4(a) to 4(c). The values of H_c are 112.5, 215, and 220 mT at 1.9 K for samples 1 to 3, respectively. In sample 1, the MR signal initially exhibits a gradual increase with an increasing magnetic field from zero, takes its maximum, and drops sharply toward H_c. This behavior is consistent with that reported in the bulk crystals [26]. These features are also observed in samples 2 and 3, while the MR drop toward H_c becomes less abrupt possibly due to the demagnetization effect. Indeed, H_c values for samples 2 and 3 are larger than that for sample 1.

In addition, a hump structure appears during the MR drop, as indicated by orange vertical arrows. In particular, this behavior is quite clear in sample 3 and has not been observed in the bulk crystals. The hysteresis of the MR signal with stepwise MR changes appears around the peak structure in sample 3, as shown in the inset of Fig. 4(c), and it was not observed in samples 1 and 2.

The magnitude of the MR reduction until H_c depends on the sample configuration as shown in Fig. 4. It is about 1% in samples 1 and 2, while it becomes 8% in sample 3, even though the shape and dimensions of the sample are almost the same in the three samples. The former two correspond to the CIP configuration [Figs. 2(a) and 2(b)], while the latter has the CPP configuration [Fig. 2(c)]. These results indicate that conduction electrons are more efficiently scattered by the helical structure formed in $YbNi_3Al_9$ crystals in the CPP configuration and its efficiency is changeable as a function of the strength of the applied magnetic field. Thus, the steep reduction of the MR toward H_c indicates that the MR is well correlated with the number of helical twists, suggesting the existence of the CSL.

A temperature dependence of the MR is shown in Figs. 4(d) to 4(f). The MR data exhibit behavior below T_c in all samples similar to that observed at 1.9 K. The value of H_c decreases with increasing temperature, as indicated by red arrow heads. The hump structure appears below T_c in samples 2 and 3, while its field range becomes smaller as the temperature approaches T_c. The MR eventually becomes featureless around T_c and shows a monotonic decrease above T_c.

Figure 5 shows the MR data of sample 3 taken with a field interval of 0.1 mT. This field increment is about ten times smaller than that used in Fig. 4. Even in micrometer-sized $YbNi_3Al_9$ samples, many stepwise changes of the MR signal are clearly seen as indicated by the horizontal and vertical black bars. The magnitude of the MR steps is of about 1 mΩ. In the case of $CrNb_3S_6$, the reduction of the sample size and the data acquisition with a fine magnetic field interval lead to a successful detection of discretized signals associated with the change of the soliton number of the CSL, as demonstrated in MR [11,14], magnetization [13,27], and resonant experiments [28].

Such stepwise MR changes appear even in the field region where the hump structure appears. The origin of hump structure is attributed to the lock-in behavior of the CSL because the normalized field value for the onset of the hump structure is similar to that at which the plateau of the CSL wave vector at $0.375q_0$ was observed by resonant x-ray scattering experiments [18]. Interestingly, after the hump structure sets in accompanying a small MR jump at 163.3 mT, the MR signals become less discretized and rather smooth. It reduces gradually up to 190.7 mT and then shows a sequence of stepwise changes toward H_c. Similar behavior is also observed from 119.2 to 132.7 mT, followed by many MR steps. These results may be

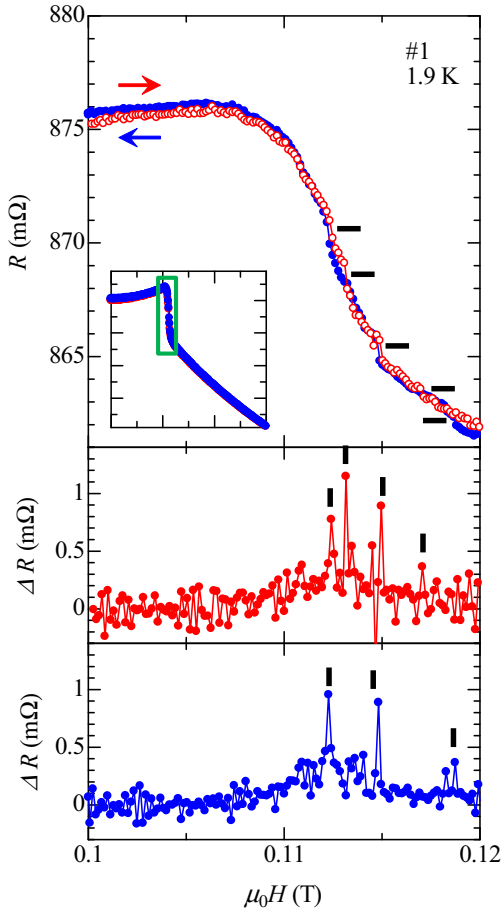

FIG. 6. MR data and their differential ΔR in a field region where the sharp negative MR appears for sample 1. The increment of the magnetic field is 0.15 mT.

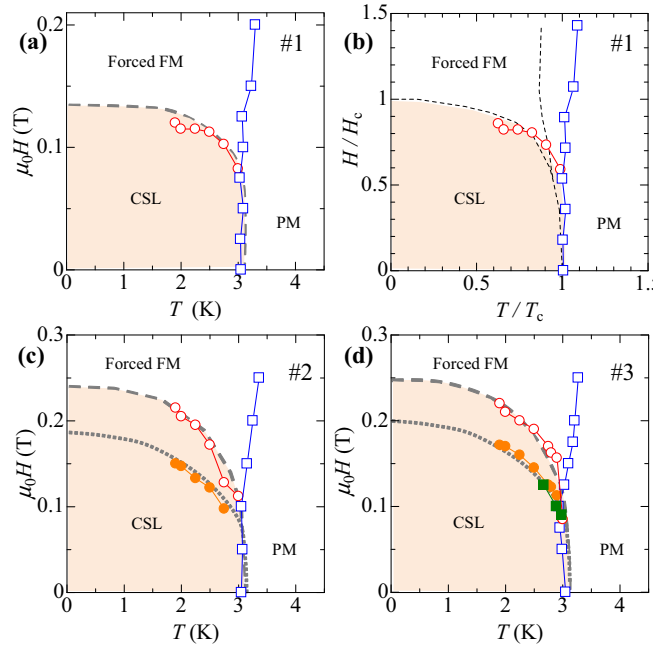

FIG. 7. (a) Magnetic phase diagram derived from electrical transport properties of the micrometer-sized $YbNi_3Al_9$ crystal (sample 1). Red open circles represent $H_c(T)$ values determined in Figs. 4(d) to 4(f), while blue open squares correspond to $T_c(H)$ values in Figs. 3(d) to 3(f). A dashed gray line serves as a guide for the eye to see the phase boundary. (b) Normalized magnetic phase diagram of sample 1. The dotted lines correspond to the phase boundaries determined by specific heat measurements of bulk $YbNi_3Al_9$ crystals [26]. (c) and (d) Magnetic phase diagrams for samples 2 and 3. In addition to $H_c(T)$ and $T_c(H)$ boundaries, the onset of the kink structure seen in Fig. 3 and the hump structure found in Fig. 4 are indicated by green solid squares and orange solid circles, respectively.

a sign of the lock-in behavior of the CSL, suggesting that the lock-in phenomena could occur more frequently.

Figure 6 shows the MR data for sample 1 taken with a field interval of 0.15 mT. Several stepwise changes of the MR signal are clearly found even in the steep negative MR region with negligibly small hysteresis. Therefore, the present data suggest that the signal resulting from the CSL formation can be successfully detected in $YbNi_3Al_9$ crystals when the experimental data are acquired with a sufficiently small field step.

Large hysteresis accompanying a sudden change of the signal appears in micrometer-sized samples of $CrNb_3S_6$ [11]. This behavior is associated with the transition from the supersaturated forced ferromagnetic to the CSL phase and explained by the scenario of the surface barrier [29]. A penetration of a single soliton into the sample is impeded by the energy barrier made on the surface. When the surface barrier disappears with a decreasing magnetic field, a bunch of solitons suddenly enters the sample. In contrast, a comparatively small hysteresis during the CSL formation was observed in $YbNi_3Al_9$. This result indicates that the surface barrier is very small and allows a smooth penetration of the single soliton into the sample. A short period of the soliton in the $YbNi_3Al_9$ system may reduce the magnitude of the surface barrier and also is favorable to inducing the lock-in phenomena between the CSL and the crystal.

C. Magnetic phase diagram

Figure 7 presents the magnetic phase diagrams of micrometer-sized $YbNi_3Al_9$ crystals constructed by the electrical resistance data. In sample 1, the value of $H_c(0)$ is determined to be 0.14 T by extrapolating the $H_c(T)$ curve toward 0 K as indicated by a dashed gray line in Fig. 7(a). This value is consistent with those for the bulk crystals which have a configuration subject to a small demagnetization effect [26]. The experimental data points appear to provide the phase boundaries between paramagnetic, forced ferromagnetic, and CSL phases. In the normalized phase diagram shown in Fig. 7(b), the observed phase boundaries are in good agreement with those obtained by specific heat measurements [19,26]. Furthermore, the phase diagram for $YbNi_3Al_9$ crystals is qualitatively consistent with that for $CrNb_3S_6$ crystals [30–32].

Note that the behavior which emanates from T_c at zero field and moves towards the upper right corner is reminiscent of B20 compounds such as MnSi [33,34], FeGe [35], and Cu_2OSeO_3 [36]. The first-order transition induced by spin fluctuations is discussed in those cubic compounds. In this respect, the nature

of the phase transition is also quite an intriguing issue in $4f$ electron system chiral magnetic materials.

The magnetic phase diagrams for samples 2 and 3 present additional data points in the CSL phase, which are due to the lock-in behavior of the MR signals. It is clear that this anomaly was also detected as a kink structure in the temperature dependence of the electrical resistance in Fig. 3(f), as seen in the phase diagram for sample 3. The locked CSL state is an interesting feature uniquely manifested in a family of the $YbNi_3Al_9$ system and its emergence depending on the doping level is worth investigating.

IV. CONCLUSION

Electrical resistance measurements were performed in the micrometer-sized samples of a rare-earth chiral magnetic crystal, $YbNi_3Al_9$. The steep negative MR behavior was observed in the vicinity of H_c, where many stepwise MR changes were found together with the lock-in behavior of the MR. These observations support the existence of the CSL in $YbNi_3Al_9$ crystals as well as in $Yb(Ni_{1-x}Cu_x)_3Al_9$. Among chiral magnets, the crystal $YbNi_3Al_9$ is the second example of a material capable of hosting the CSL. Following $CrNb_3S_6$ crystals, discretized MR signals were observed and identified as a signature of the CSL formation in $YbNi_3Al_9$ crystals. Nevertheless, different features of MR signals in terms of hysteresis require further experimental studies and theoretical considerations of the physical picture of the microscopic mechanism of the exchange interactions as well as the scattering process of conduction electrons on chiral magnetic phases in the $4f$ electron system, which would lead to a comprehensive understanding of chiral magnetism.

ACKNOWLEDGMENTS

We thank Y. Kato and J. Kishine for useful discussions and F. J. T. Goncalves for a critical reading of the manuscript. We acknowledge support from Grants-in-Aid for Scientific Research (Grants No. 25220803, No. 17H02767, and No. 17H0923, No. JP16H01073) and JSPS Core-to-Core Program "Advanced Research Networks".

[1] I. Dzyaloshinskii, J. Phys. Chem. Solids **4**, 241 (1958).
[2] T. Moriya, Phys. Rev. **120**, 91 (1960).
[3] I. Dzyaloshinskii, Sov. Phys. JETP **19**, 960 (1964).
[4] Y. A. Izyumov, Sov. Phys.-Usp. **27**, 845 (1984).
[5] J. Kishine, K. Inoue, and Y. Yoshida, Prog. Theor. Phys. Suppl. **159**, 82 (2005).
[6] A. Bogdanov and D. Yablonskii, Zh. Eksp. Teor. Fiz. **95**, 178 (1989).
[7] Y. Togawa, T. Koyama, K. Takayanagi, S. Mori, Y. Kousaka, J. Akimitsu, S. Nishihara, K. Inoue, A. S. Ovchinnikov, and J. Kishine, Phys. Rev. Lett. **108**, 107202 (2012).
[8] S. Mühlbauer, B. Binz, F. Jonietz, C. Pfleiderer, A. Rosch, A. Neubauer, R. Georgii, and P. Böni, Science **323**, 915 (2009).
[9] X. Z. Yu, N. Kanazawa, Y. Onose, K. Kimoto, W. Z. Zhang, S. Ishiwata, Y. Matsui, and Y. Tokura, Nat. Mater. **10**, 106 (2010).
[10] D. McGrouther, R. J. Lamb, M. Krajnak, S. McFadzean, S. McVitie, R. L. Stamps, A. O. Leonov, A. N. Bogdanov, and Y. Togawa, New J. Phys. **18**, 095004 (2016).
[11] Y. Togawa, T. Koyama, Y. Nishimori, Y. Matsumoto, S. McVitie, D. McGrouther, R. L. Stamps, Y. Kousaka, J. Akimitsu, S. Nishihara, K. Inoue, I. G. Bostrem, V. E. Sinitsyn, A. S. Ovchinnikov, and J. Kishine, Phys. Rev. B **92**, 220412 (2015).
[12] A. Neubauer, C. Pfleiderer, B. Binz, A. Rosch, R. Ritz, P. G. Niklowitz, and P. Böni, Phys. Rev. Lett. **102**, 186602 (2009).
[13] K. Tsuruta, M. Mito, Y. Kousaka, J. Akimitsu, J. Kishine, Y. Togawa, H. Ohsumi, and K. Inoue, J. Phys. Soc. Jpn. **85**, 013707 (2016).
[14] J.-I. Yonemura, Y. Shimamoto, T. Kida, D. Yoshizawa, Y. Kousaka, S. Nishihara, F. J. T. Goncalves, J. Akimitsu, K. Inoue, M. Hagiwara, and Y. Togawa, Phys. Rev. B **96**, 184423 (2017).
[15] L. Wang, N. Chepiga, D.-K. Ki, L. Li, F. Li, W. Zhu, Y. Kato, O. S. Ovchinnikova, F. Mila, I. Martin, D. Mandrus, and A. F. Morpurgo, Phys. Rev. Lett. **118**, 257203 (2017).
[16] M. N. Wilson, E. A. Karhu, D. P. Lake, A. S. Quigley, S. Meynell, A. N. Bogdanov, H. Fritzsche, U. K. Rößler, and T. L. Monchesky, Phys. Rev. B **88**, 214420 (2013).
[17] N. Kanazawa, J. S. White, H. M. Rønnow, C. D. Dewhurst, Y. Fujishiro, A. Tsukazaki, Y. Kozuka, M. Kawasaki, M. Ichikawa, F. Kagawa, and Y. Tokura, Phys. Rev. B **94**, 184432 (2016).
[18] T. Matsumura, Y. Kita, K. Kubo, Y. Yoshikawa, S. Michimura, T. Inami, Y. Kousaka, K. Inoue, and S. Ohara, J. Phys. Soc. Jpn. **86**, 124702 (2017).
[19] H. Ninomiya, T. Sato, K. Inoue, and S. Ohara, Physica B **536**, 654 (2018).
[20] S. Okumura, Y. Kato, and Y. Motome, J. Phys. Soc. Jpn. **87**, 033708 (2018).
[21] Y. Kousaka *et al.* (unpublished).
[22] R. E. Gladyshevskii, K. Cenzual, H. D. Flack, and E. Parthé, Acta Crystallogr., Sect. B: Struct. Sci. **49**, 468 (1993).
[23] S. Ohara, T. Yamashita, Y. Mori, and I. Sakamoto, J. Phys.: Conf. Ser. **273**, 012048 (2011).
[24] S. Ohara, S. Fukuta, K. Ohta, H. Kono, T. Yamashita, Y. Matsumoto, and J. Yamamura, JPS Conf. Proc. **3**, 017016 (2014).
[25] T. Hirayama, K. Matsubayashi, T. Yamashita, S. Ohara, K. Munakata, and Y. Uwatoko, J. Phys.: Conf. Ser. **391**, 012020 (2012).
[26] R. Miyazaki, Y. Aoki, R. Higashinaka, H. Sato, T. Yamashita, and S. Ohara, Phys. Rev. B **86**, 155106 (2012).
[27] K. Tsuruta, M. Mito, Y. Kousaka, J. Akimitsu, J. Kishine, Y. Togawa, and K. Inoue, J. Appl. Phys. **120**, 143901 (2016).
[28] F. J. T. Goncalves, T. Sogo, Y. Shimamoto, Y. Kousaka, J. Akimitsu, S. Nishihara, K. Inoue, D. Yoshizawa, M. Hagiwara, M. Mito, R. L. Stamps, I. G. Bostrem, V. E. Sinitsyn, A. S. Ovchinnikov, J. Kishine, and Y. Togawa, Phys. Rev. B **95**, 104415 (2017).
[29] M. Shinozaki, Y. Masaki, R. Aoki, Y. Togawa, and Y. Kato, Phys. Rev. B **97**, 214413 (2018).

[30] Y. Togawa, Y. Kousaka, S. Nishihara, K. Inoue, J. Akimitsu, A. S. Ovchinnikov, and J. Kishine, Phys. Rev. Lett. **111**, 197204 (2013).

[31] K. Tsuruta, M. Mito, H. Deguchi, J. Kishine, Y. Kousaka, J. Akimitsu, and K. Inoue, Phys. Rev. B **93**, 104402 (2016).

[32] E. M. Clements, R. Das, L. Li, P. J. Lampen-Kelley, M.-H. Phan, V. Keppens, D. Mandrus, and H. Srikanth, Sci. Rep. **7**, 6545 (2017).

[33] Y. Ishikawa and M. Arai, J. Phys. Soc. Jpn. **53**, 2726 (1984).

[34] C. Thessieu, C. Pfleiderer, A. N. Stepanov, and J. Flouquet, J. Phys.: Condens. Matter **9**, 6677 (1997).

[35] H. Wilhelm, M. Baenitz, M. Schmidt, U. K. Rößler, A. A. Leonov, and A. N. Bogdanov, Phys. Rev. Lett. **107**, 127203 (2011).

[36] I. Živković, J. S. White, H. M. Rønnow, K. Prša, and H. Berger, Phys. Rev. B **89**, 060401 (2014).